may also play an important role in the stabilization of monomers containing $[(P_5)_2M]^z$ units. On this basis, it seems possible that a wide variety of other charged decaphosphametallocenes and related carbon-free sandwich complexes (*45*) may be accessible species.

References and Notes

1. T. J. Kealy, P. L. Pauson, *Nature* **168**, 1039 (1951).
2. S. A. Miller, J. A. Tebboth, J. F. Tremaine, *J. Chem. Soc.*, 632 (1952).
3. R. B. Woodward, M. Rosenblum, M. C. Whiting, *J. Am. Chem. Soc.* **74**, 3458 (1952).
4. A. Togni, R. L. Halterman, Eds., *Metallocenes: Synthesis, Reactivity, Applications* (Wiley-VCH, Weinheim, Germany, 1998).
5. N. J. Long, *Metallocenes* (Blackwell Science, Oxford, UK, 1998).
6. A. D. Garnovskii, A. P. Sadimenko, M. I. Sadimenko, D. A. Garnovskii, *Coord. Chem. Rev.* **173**, 31 (1998).
7. K. B. Dillon, F. Mathey, J. F. Nixon, *Phosphorus: The Carbon Copy* (Wiley, Chichester, UK, 1998).
8. R. Bartsch, P. B. Hitchcock, J. F. Nixon, *J. Chem. Soc. Chem. Commun.* **1987**, 1146 (1987).
9. ———, *J. Organomet. Chem.* **356**, C1 (1988).
10. P. B. Hitchcock, J. F. Nixon, R. M. Matos, *J. Organomet. Chem.* **490**, 155 (1995).
11. T. Clark *et al.*, *Angew. Chem. Int. Ed.* **39**, 2087 (2000).
12. R. Bartsch *et al.*, *J. Organomet. Chem.* **529**, 375 (1997).
13. F. G. N. Cloke, J. R. Hanks, P. B. Hitchcock, J. F. Nixon, *Chem. Commun.* **1999**, 1731 (1999).
14. F. G. N. Cloke, J. C. Green, J. R. Hanks, J. F. Nixon, J. L. Suter, *J. Chem. Soc. Dalton Trans.* **2000**, 3534 (2000).
15. R. Bartsch *et al.*, *J. Chem. Soc. Dalton Trans.* **2001**, 1013 (2001).
16. M. Al-Ktaifani, J. C. Green, P. B. Hitchcock, J. F. Nixon, *J. Chem. Soc. Dalton Trans.* **2001**, 1726 (2001).
17. M. Baudler *et al.*, *Angew. Chem. Int. Ed. Engl.* **27**, 280 (1988).
18. O. J. Scherer, *Angew. Chem. Int. Ed. Engl.* **29**, 1104 (1990).
19. E. J. P. Malar, *J. Org. Chem.* **57**, 3694 (1992).
20. A. Dransfeld, L. Nyulaszi, P. v. R. Schleyer, *Inorg. Chem.* **37**, 4413 (1998).
21. M. Baudler, T. Etzbach, *Angew. Chem. Int. Ed. Engl.* **30**, 580 (1991).
22. O. J. Scherer, *Acc. Chem. Res.* **32**, 751 (1999).
23. ———, H. Swarowsky, G. Wolmershäuser, W. Kaim, S. Kohlmann, *Angew. Chem. Int. Ed. Engl.* **26**, 1153 (1987).
24. J. E. Ellis, D. W. Blackburn, P. Yuen, M. Jang, *J. Am. Chem. Soc.* **115**, 11616 (1993).
25. Details of the syntheses, isolation, and characterization of the $[K(18\text{-Crown-6})]^+$, $(Ph_3P)_2N^+$, and Ph_4P^+ salts of **1** are available on *Science* Online (*46*).
26. Electrochemical characterization of $[Cp^*FeP_5]^-$ has been reported by R. F. Winter and W. E. Geiger [*Organometallics* **18**, 1827 (1999)].
27. D. F. Evans, *J. Chem. Soc.*, 2003 (1959).
28. Crystallographic details are available on *Science* Online (*46*).
29. L. Weber, *Chem. Rev.* **92**, 1839 (1992).
30. O. J. Scherer, T. Hilt, G. Wolmershäuser, *Organometallics* **17**, 4110 (1998).
31. T. P. Hamilton, Henry F. Schaefer III, *Angew. Chem. Int. Ed. Engl.* **28**, 485 (1989).
32. M. D. Fryzuk, T. S. Haddad, D. J. Berg, *Coord. Chem. Rev.* **99**, 137 (1990).
33. J. Perdew, Y. Wang, *Phys. Rev. B* **45**, 13244 (1992).
34. K. Burke, J. P. Perdew, Y. Wang, *Electronic Density Functional Theory. Recent Progress and New Directions*, J. F. Dobson, G. Vignale, M. P. Das, Eds. (Plenum, New York, 1998).
35. C. Adamo, V. Barone, *J. Chem. Phys.* **108**, 664 (1998).
36. W. J. Hehre, L. Radom, P. v. R. Schleyer, J. A. Pople, *Ab Initio Molecular Orbital Theory* (Wiley, New York, 1986).
37. R. Stowasser, R. Hoffmann, *J. Am. Chem. Soc.* **121**, 3414 (1999).
38. C. Elschenbroich, A. Salzer, *Organometallics* (Wiley-VCH, Weinheim, Germany, ed. 1, 1989).
39. A. Haaland, *Acc. Chem. Res.* **12**, 415 (1979).
40. M. Bochmann, *Organometallics* (Oxford Chemistry Primers, Oxford Univ. Press, Oxford, New York, 1994), vol. 2.
41. K. L. T. Wong, H. H. Brintzinger, *J. Am. Chem. Soc.* **97**, 5143 (1975).
42. F. W. S. Benfield, M. L. H. Green, J. S. Ogden, D. Young, *J. Chem. Soc. Chem. Commun.* **1973**, 866 (1973).
43. D. W. Blackburn, D. Britton, J. E. Ellis, *Angew. Chem. Int. Ed.* **31**, 1495 (1992).
44. M. Baudler, D. Düster, D. Ouzounis, *Z. Anorg. Allg. Chem.* **544**, 87 (1987).
45. M. Lein, J. Frunzke, A. Timoshkin, G. Frenking, *Chem. Eur. J.* **7**, 4155 (2001).
46. Supplementary data are available on *Science* Online at www.sciencemag.org/cgi/content/full/295/5556/832/DC1.

47. Dedicated to Professor Marianne Baudler on the occasion of her 80th birthday. We are grateful to the National Science Foundation (J.E.E.) and the donors of the Petroleum Research Fund administrated by the American Chemical Society (J.E.E.) for financial support of this work. We acknowledge B. Chen for the solid-state ^{31}P-NMR spectral measurements.

22 October 2001; accepted 27 December 2001

Aerosol Effect on Cloud Droplet Size Monitored from Satellite

Francois-Marie Bréon,[1]* Didier Tanré,[2] Sylvia Generoso[1]

Aerosol concentration and cloud droplet radii derived from space-borne measurements are used to explore the effect of aerosols on cloud microphysics. Cloud droplet size is found to be largest (14 micrometers) over remote tropical oceans and smallest (6 micrometers) over highly polluted continental areas. Small droplets are also present in clouds downwind of continents. By using estimates of droplet radii coupled with aerosol load, a statistical mean relationship is derived. The cloud droplet size appears to be better correlated with an aerosol index that is representative of the aerosol column number under some assumptions than with the aerosol optical thickness. This study reveals that the effect of aerosols on cloud microphysics is significant and occurs on a global scale.

Aerosols may reduce the degree of Earth global warming resulting from the increase of greenhouse gases in the atmosphere (*1*, *2*). They directly impact the radiative balance of Earth through a net increase of its albedo, particularly over the oceans (*3*, *4*). Aerosols can also act as cloud condensation nuclei (CCN), increasing the number of droplets in clouds, which tends to decrease the mean droplet size and may increase the cloud albedo (*5*), depending on the aerosol absorption and cloud optical thickness (*6*). This process, referred to as the "Twomey effect" or the "first indirect" aerosol radiative forcing, has a net cooling effect on climate. A direct demonstration of the aerosol effect on cloud albedo was provided by the observation of lines of larger reflectance in cloud fields identified as tracks of ship exhaust (*7*). Indirect observations of this effect can also be made by comparing cloud droplet size and aerosol concentration. Cloud droplet effective radii were derived by using global scale AVHRR (advanced very high resolution radiometer) measurements (*8*). The results of a global application (*9*) indicate a contrast in cloud droplet size of about 2 μm over land and ocean surfaces, as well as a hemispheric contrast of 1 μm, both of which support the Twomey hypothesis. Similar patterns of the aerosol optical thickness and the cloud droplet effective radius, derived from AVHRR measurements, have been observed over the oceans (*10*). Cases of reduced droplet radii and suppression of rain—the second indirect aerosol effect—in areas of high aerosol load were identified on satellite imagery (*11*, *12*). Furthermore, several in situ measurements have shown a relationship between the aerosol concentration and the cloud droplet size distribution (*13*–*15*).

The polarization and directionality of the earth reflectances (POLDER) instrument (*16*) is well suited for assessing the Twomey hypothesis globally, because its measurements provide a unique opportunity to measure cloud droplet effective radius (hereafter referred to as CDR) (*17*), as well as aerosol loading (*18*), over both land and ocean surfaces. The POLDER radiometer was launched aboard the Advanced Earth-Observing Satellite (ADEOS) in August 1996. Continuous monitoring of the solar radiation reflected by the earth, including its polarization and directional signatures, started on 30 October 1996, and ended on 30 June 1997, with the unexpected failure of the satellite solar panel. Monthly maps were generated of an

[1]Laboratoire des Sciences du Climat et de l'Environnement, Commissariat à l'Energie Atomique, Gif sur Yvette, France. [2]Laboratoire d'Optique Atmosphérique, CNRS, Université des Sciences et Technologies de Lille, Villeneuve d'Ascq, France.

*To whom correspondence should be addressed. E-mail: fmbreon@cea.fr

"aerosol index" that quantifies the atmospheric load by small particles (*19*). Under some assumptions, the aerosol index is expected to be proportional to the aerosol column number when the widely used optical thickness is proportionally more sensitive to the large particle fraction (*20*). Spatial and temporal distribution of the index indicate that it is mostly sensitive to aerosols generated by biomass burning and human-generated pollution (*21*). Similarly, the polarization signature of liquid water clouds was used to derive monthly mean estimates of CDR (*22*).

A seasonal (March-May) average of these two parameters, aerosol index and CDR, is illustrated in Figs. 1 and 2. The highest values of the aerosol index (Fig. 1) are observed over southeast Asia and India, as well as Central Africa. These presumably reflect the presence of anthropogenic aerosols from industrial activity and biomass burning. Relatively large values are also observed over the sub-Sahelian region, Central America, and Eastern Europe. Very low values are apparent over the open oceans. There is a significant land-ocean contrast. The influence of continental aerosols over the ocean is notable, particularly downwind of regions with high aerosol loading (winds are mostly westward in the tropics, and eastward in mid-latitude regions). Over the oceans, the highest values are observed east of China, over the northern part of the Indian Ocean, downwind of the Sahel, and surrounding Central America. Note also that the atmosphere over southern oceans appears cleaner than over the basins of the Northern Hemisphere.

Cloud droplet radius estimates (Fig. 2) are based on the angular signature of the polar-

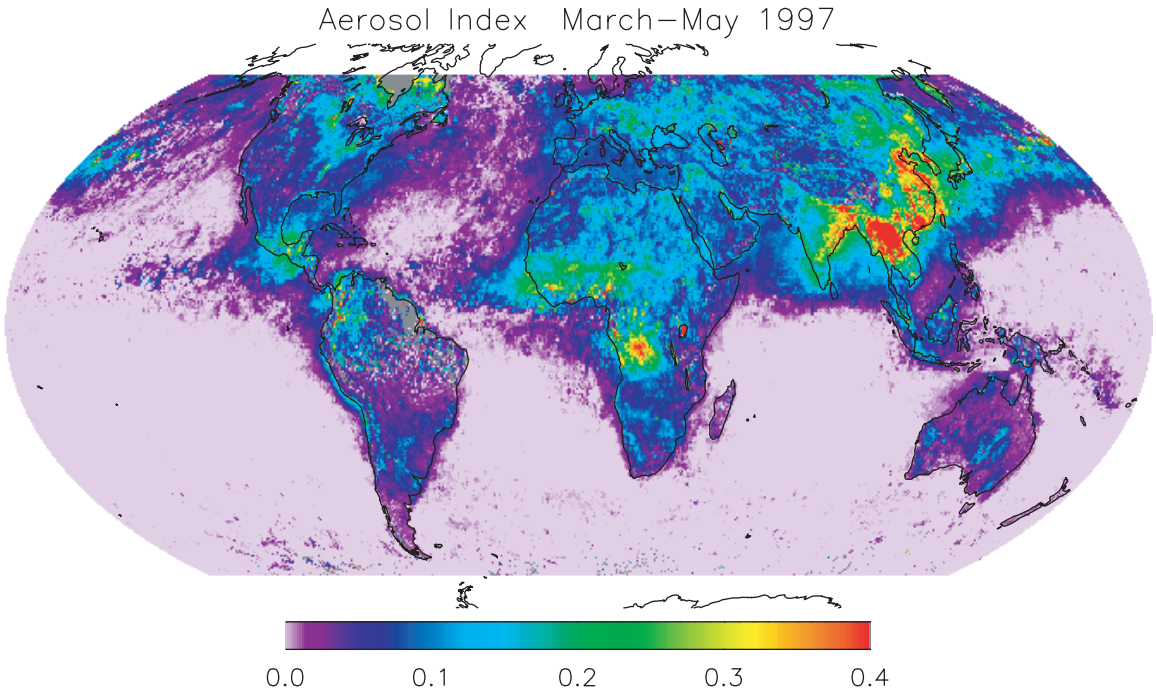

Fig. 1. Aerosol index derived from POLDER measurements during the spring of 1997. The aerosol index quantifies the atmospheric loading by small particles.

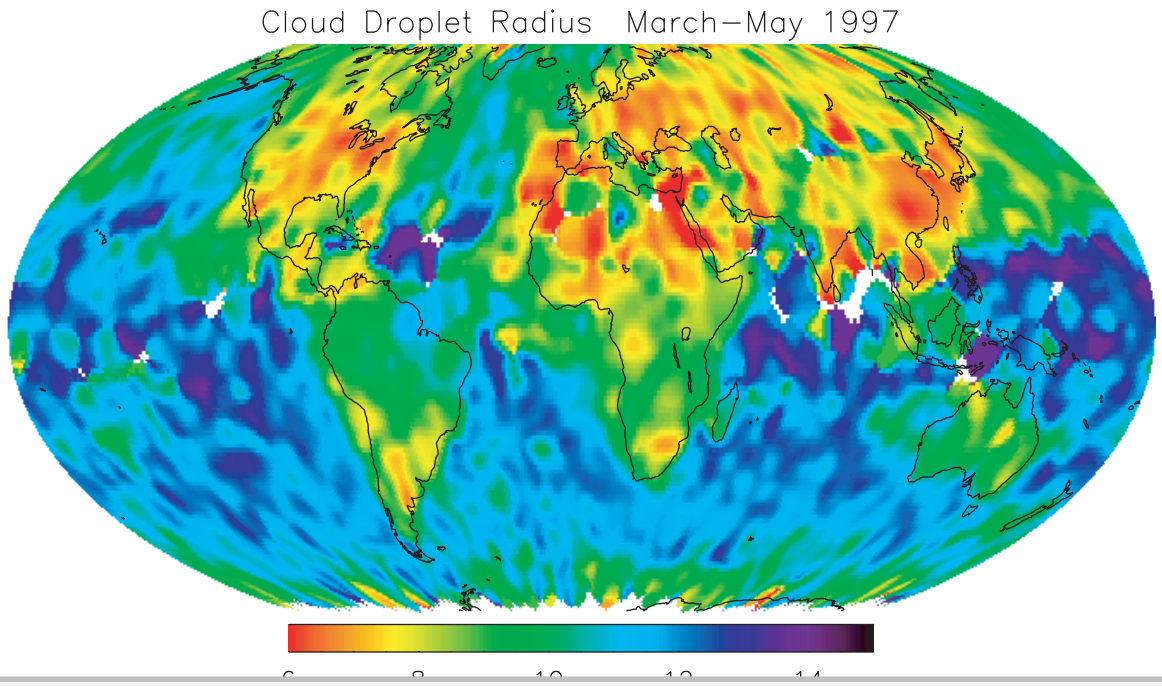

Fig. 2. Cloud droplet radius derived from POLDER measurements during the spring of 1997. The units are microns. White areas correspond to regions where no successful estimate was possible. This image is based upon a compilation of 19,500 estimates.

ized radiance reflected by a cloud field (*17*). This estimate requires a specific viewing geometry and is only possible when the cloud field is relatively uniform over an area of approximately 150 × 150 km^2 and when the cloud droplet size distribution is narrow. When these conditions are met, the retrieval is highly reliable with no identified cause for bias (*23*). The seasonal composite of CDR for the spring of 1997 is shown in Fig. 2. Despite the natural variability, coherent patterns are clearly depicted. Many spatial features are similar to those found in the aerosol index; namely, the smallest CDR values are found over regions of high aerosol index, and the largest values are over the open oceans where the atmosphere is very clean: CDR is between 6 and 10 μm over land surfaces, values over the oceans vary between 12 and 14 μm in remote areas down to the same low values of 6 μm in regions with the highest aerosol index. CDR over areas downwind of land surfaces is clearly affected by continental influences.

A latitudinal gradient is apparent in the southern ocean with smaller droplets occurring toward the pole. This result agrees with previous in situ measurements that showed CDR much smaller in polar stratocumulus clouds than in mid-latitude clouds (*24*). This effect, however, cannot be presently attributed to the presence of aerosols, because this area is known to be very clean, as confirmed by the low aerosol index values. The gradient is apparent during other months, in particular during the December-to-February period when the solar elevation allows observations in the southernmost latitudes (*22*). The corresponding latitudinal gradient is not apparent in the Northern Hemisphere, presumably because the aerosol impact is then dominant.

The similarities between the spatial distributions of aerosol index and CDR suggest that a more quantitative analysis can be performed. The two estimates are not fully coincident, because the presence of clouds makes the quantitative monitoring of aerosol impossible with a passive technique. Thus, the individual measurements that are used to derive the two seasonal fields may correspond to different meteorological situations. A quantitative analysis requires the use of individual estimates rather than temporal means. In this study, for each individual estimate of CDR, a back-trajectory was computed up to a location where an aerosol index value was available. This procedure yields sets (CDR, aerosol load) that are based on individual and quasi coincident observations. The back-trajectory makes use of the six hourly wind fields from the European Center for Medium-Range Weather Forecast (ECMWF) at 850 hPa, and was limited in time (24 hours) and space (1000 km). Here, we assume that the aerosol estimate remains valid

the sets were obtained from measurements closer than 100 km in space. The study area was restricted to 60°N to 45°S to limit the impact of the latitudinal gradient observed in the Southern Hemisphere that clearly results from a different cloud process than the one analyzed here. Because most significant sources of aerosols are within these boundaries as confirmed by previous studies (*25*), this region is well suited to explorations of the effect of aerosols on cloud microphysics.

As a result of this procedure a total of 44,066 valid (CDR, aerosol index) sets were available for further analysis, of which 28,686 aerosol estimates were derived from oceanic measurements, and 15,380 from land observations. Recall that the respective algorithms make use of different techniques, and that the results derived over the ocean are more accurate than the ones obtained over land.

The mean and standard deviation of CDRs were computed for sets with a given aerosol index (bins of 0.025; 0.0125 for the first two bins) and while distinguishing between aerosol estimates derived over land and over the ocean (Fig. 3). The curves confirm the relationship apparent on the seasonal maps. On average, CDR is smaller when the aerosol load is larger. Because there is a clear physical process that predicts such a decrease, this observed correlation can be interpreted as a causal connection. The aerosols clearly impact the cloud microphysics, not only for specific cases, as in situ and airborne measurements have already shown, but also on a global scale. The aerosol effect on cloud microphysics appears nonlinear: the change in CDR with aerosol index (the derivative) is larger for clean atmospheres than for those with a significant load as already noted in specific cases (*11*).

The statistical significance of the CDR mean is illustrated by the error bars on the *y* axis. They represent the confidence level of the mean value, i.e., $\sigma/\sqrt{n-2}$, where n and σ are the number of CDR measurements within the bin and their standard deviation, if one assumes independent data. Although the observations show a wide range of CDR, the large number of measurements for relatively clean atmospheric areas make the corresponding mean values highly significant.

In the interpretation of the results, one must emphasize that the uncertainty on individual measurements of aerosol index is significant in regard to the *x*-axis scale in Fig. 3. This uncertainty is larger over land than over the oceans because of the large and variable land surface contribution to the measured radiance. The noise in the aerosol load estimates tends to smooth the curves in Fig. 3 and thus to decrease the apparent impact of the aerosol to the cloud microphysics (*26*). This may explain the apparent lower impact than over oceanic surfaces. It may also explain the divergence in CDR between ocean and land curves for the smallest values of aerosol index. On the other hand, it is possible that land surfaces naturally generate a low level of aerosol that is not within the capabilities of space-borne passive remote sensing. Thus a "clean" continental atmosphere would not be as pristine as an oceanic one, resulting in a smaller CDR.

The mean slope of the aerosol index–CDR relationship is highly significant for the clean cases, up to an aerosol index of 0.15 to 0.20, as shown by the small error bars. The constant mean CDR observed for aerosol indices greater than 0.15 indicates a saturation effect, although an extension of Twomey's hypothesis as suggested by (*27*) cannot be rejected. Fluctuations observed above the threshold of 0.15 are not statistically significant because of a limited number of samples.

Because the optical thickness is widely used to characterize the particle concentration, we show the result of a similar processing when the optical thickness rather than the aerosol index is used (Fig. 3). This is limited to ocean observations, because an accurate estimate from POLDER measurements is not possible over land (*19*). Recall that the aero-

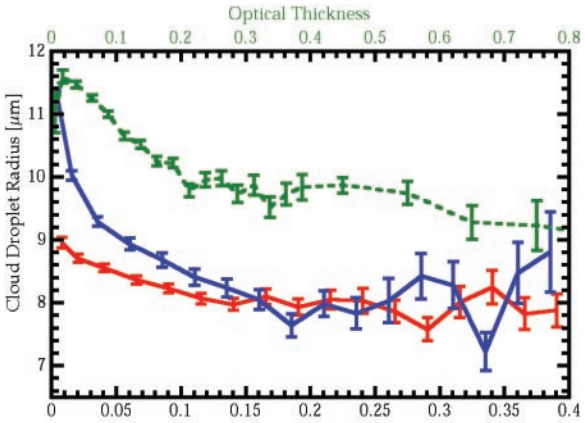

Fig. 3. Mean CDR as a function of aerosol load. The two lower curves show the mean CDR as a function of the aerosol index (lower scale) for land (red) and ocean (blue) retrievals. The upper curve is the same as the latter but as a function of optical thickness (upper scale). The error bars represent the confidence level of the mean value, i.e., $\sigma/\sqrt{n-2}$, where n and σ are the number of CDR measurements within the bin and their standard deviation.

sol index is roughly proportional to the aerosol column number when the optical thickness is affected by the presence of large particles even in limited number, which puts a large weight to the large particle fraction. As shown by the comparison of the blue and green curves (*28*) in Fig. 3, CDR is more sensitive to the aerosol index than to the optical thickness, which is to be expected, because the aerosol index is a function of the CCN concentration. Aerosol characteristics other than typical size (for instance, their hygroscopicity) may affect the statistical results of Fig. 3.

We now compare the observed statistical relationship to the simple theory originally proposed by Twomey. The number of aerosol particles that may act as CCN, N_a, and the number of cloud droplets, N_d, are approximately related through (*29*):

$$N_d \approx (N_a)^{\alpha} \quad (1)$$

Cloud process models and measurements indicate that α is on the order of 0.7. If one assumes a constant liquid water content, these numbers are related to the cloud droplet effective radius through (*5, 6, 27*):

$$\partial \log(r) = \frac{\partial \log(N_d)}{3}$$

$$= \frac{\alpha}{3}\partial \log(N_a) = \frac{\alpha}{3}\partial \log(AI) \quad (2)$$

Thus, a slope of ≈0.23 is expected between the mean radius and the aerosol index on a log-log scale. Figure 4 shows the corresponding plot. Our analysis can be seen as supporting Twomey's hypothesis: There is a linear relationship (in log scale) between a change in aerosol concentration and a change in cloud droplet radius. On the other hand, the value of the slope is much smaller than the 0.23 expected: 0.085 over the oceans and 0.04 over land. The value found here for the oceanic cases is very similar to the one that can be derived from AVHRR data (*20*) and in the range of recent modeling results (*27*).

The results of this study clearly demonstrate a significant impact of aerosols on cloud microphysics at the global scale; however, several limitations discussed below prevent a definite quantitative interpretation of their indirect radiative forcing.

1) The constraints on the CDR retrieval, in particular the spatial homogeneity and the narrow size-distribution criteria, may select particular cloud types (stratiform rather than convective) and/or a specific time in the cloud life cycle. Therefore, the relationship may not be valid for all cloud types and may be biased toward sensitive or insensitive clouds.

2) The parameter of importance for the Twomey effect is the concentration of CCN in the atmospheric layer where cloud droplets are formed. The POLDER retrievals measure an aerosol load index integrated over the vertical, not the CCN concentration. This is a source of uncertainty in the aerosol index–CDR relationship, although it is reasonable to assume that the CCN concentration and the aerosol index are well correlated, because the latter is proportional to the column aerosol number.

The observed relationship of Figs. 3 and 4 is clearly not a spurious result of the inversion algorithms. Although over land surfaces both the aerosol and cloud inversions make use of the polarized radiance measurements, the former is based on the magnitude of the radiance; the latter uses its directional signature. We cannot identify any mechanism in the satellite estimates that would generate a misleading relationship between CDR and the aerosol index. Moreover, the aerosol inversion technique over the oceans is based on the radiance measurement, with limited contribution from polarization.

Because of the various limitations of the remote sensing techniques and the inherent statistical aspect of our results, it is not possible to reliably quantify the aerosol first indirect radiative effect on climate. Nevertheless, the present results provide evidence of a strong effect of aerosols on cloud microphysics at the global scale and allow the quantification of the effect's magnitude over land and ocean. The observed mean relationship can be used to validate the aerosol-cloud physical mechanisms implemented in models.

Whether the observed impact on cloud microphysics is of anthropogenic origin is a question of importance. The satellite measurement cannot unambiguously distinguish natural and human-generated aerosols. However, the analysis of the spatial and temporal patterns in the aerosol index monthly maps strongly suggests that the bulk of the aerosol load originates from slash-and-burn agriculture practices and from highly polluted areas (*25*). A large fraction of the observed aerosol effect on clouds is probably an anthropogenic impact.

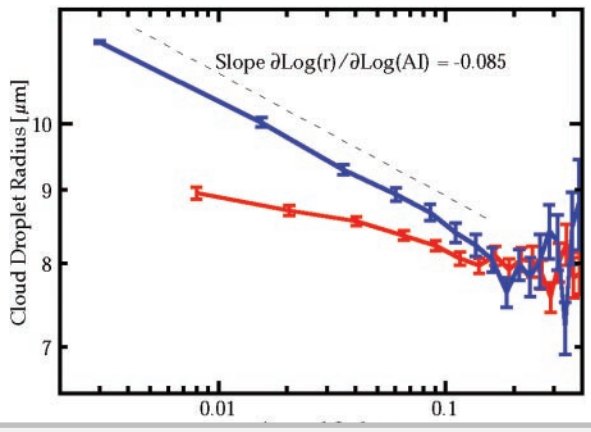

Fig. 4. Same as Fig. 3 on a log-log scale. Only the curves as a function of aerosol index are shown.

References and Notes

1. J. E. Penner *et al.*, *Bull. Am. Meteorol. Soc.* **75**, 375 (1994).
2. R. J. Charlson *et al.*, *Science* **255**, 423 (1992).
3. J. Haywood, V. Ramaswamy, B. Soden, *Science* **283**, 1299 (1999).
4. O. Boucher, D. Tanré, *Geophys Res. Lett.* **27**, 1103 (2000).
5. S. Twomey, *J. Atmos. Sci.* **34**, 1149 (1977).
6. Y. J. Kaufman, R. S. Fraser, *Science* **277**, 1636 (1997).
7. J. A. Coakley, R. L. Bernstein, P. A. Durkee, *Science* **237**, 1020 (1987).
8. T. Nakajima, M. D. King, *J. Atmos. Sci.* **47**, 1878 (1990).
9. Q. Han, W. B. Rossow, A. A. Lacis, *J. Clim.* **7**, 465 (1994).
10. M. A. Wetzel, L. L. Stowe, *J. Geophys. Res.* **104**, 31287 (1999).
11. D. Rosenfeld, *Science* **287**, 1793 (2000).
12. _____, *Geophys. Res. Lett.* **26**, 3105 (1999).
13. R. J. Vong, D. S. Covert, *J. Atmos. Sci.* **55**, 2180 (1998).
14. G. M. Frick, W. A. Hoppel, *Bull. Am. Meteorol. Soc.* **74**, 2195 (1993).
15. J. R. Snider, J.-L. Brenguier, *Tellus* **52**, 828 (2000).
16. P.-Y. Deschamps *et al.*, *IEEE Trans. Geosci. Remote Sens.* **32**, 598 (1994).
17. F.-M. Bréon, Ph. Goloub, *Geophys. Res. Lett.* **25**, 1879 (1998).
18. M. Herman *et al.*, *J. Geophys. Res.* **102**, 17039 (1997).
19. Over land surfaces, the aerosol index is inferred from the polarized radiance that is not fully related to the aerosol optical thickness. Because large particles yield negligible polarization, the index quantifies the load of the accumulation mode, with an effective radius of 0.18 μm. Over the oceans, the aerosol index is defined as the product of the aerosol optical thickness and the Ångström coefficient α. α is close to zero for large particles such as dust, and on the order of 1 to 1.5 for smaller particles such as those generated by biomass burning or industrial activity. The consistency of the index over land and oceans is demonstrated by the observed continuity at the coastal boundaries.
20. T. Nakajima *et al.*, *Geophys Res. Lett.* **28**, 1171 (2001). For a given optical thickness, the number of particles is much larger for a sub-micronic aerosol (typical for biomass burning smoke and pollution) than for larger sized particles such as dust. On the other hand, the Ångström coefficient decreases as the particle size increases. Thus, the aerosol index (optical thickness × angström coefficient) partly compensates the size effects and is better related than the optical thickness to the number of particles.
21. J.-L. Deuzé *et al.*, *J. Geophys. Res.* **106**, 4913 (2001).
22. F.-M. Bréon, S. Colzy, *Geophys. Res. Lett.* **27**, 4065 (2000).
23. No ground truth validation has been performed, but the agreement between the measured and modeled polarized radiances suggests an RMS accuracy better

monthly averages also results from the natural variability when few measurements are available.
24. G. F. Herman, J. Curry, *J. Clim. Appl. Meteorol.* **23**, 5 (1984).
25. D. Tanré *et al.*, *Geophys. Res. Lett.*, **28**, 4555 (2001).
26. Each point in Fig. 3 shows the average of individual CDR measurements that correspond to a given bin of aerosol load estimates. Because there is a significant uncertainty on the aerosol load, this average is derived from cases with actual loads that may be higher or lower than the bin value. For the lowest load bin, only higher loads (smaller CDR) contaminate the estimate. This tends to decrease the average CDR all the more that the uncertainty on the aerosol load is larger.
27. G. Feingold *et al.*, *J. Geophys. Res.* **106**, 22907 (2001).
28. Because the curve as a function of optical thickness (green) is significantly above that as a function of aerosol index (blue), one may get the false impression that they have been obtained from different sets of CDR and aerosol retrievals. In fact, more than half of aerosol index estimates fall into the lowest load bin when the corresponding optical thicknesses are distributed over a wider range of values. The blue and green curves have been derived from the same sample and have the same overall mean CDR.
29. S. Twomey, in *Atmospheric Aerosols* (Elsevier Science, New York, 1977); see in particular equations 4 to 15.

20 September 2001; accepted 3 January 2002

Evidence for Strengthening of the Tropical General Circulation in the 1990s

Junye Chen,[1,2]* Barbara E. Carlson,[2] Anthony D. Del Genio[2]

Satellite observations suggest that the thermal radiation emitted by Earth to space increased by more than 5 watts per square meter, while reflected sunlight decreased by less than 2 watts per square meter, in the tropics over the period 1985–2000, with most of the increase occurring after 1990. By analyzing temporal changes in the frequency of occurrence of emitted thermal and reflected solar fluxes, the effects of El Niño–Southern Oscillation are minimized, and an independent longer-time-scale variation of the radiation budget is identified. Similar analyses of upper tropospheric humidity, cloud amount, surface air temperature, and vertical velocity confirm that these flux changes are associated with a decadal-time-scale strengthening of the tropical Hadley and Walker circulations. Equatorial convective regions have intensified in upward motion and moistened, while both the equatorial and subtropical subsidence regions have become drier and less cloudy.

The energy exchange between Earth and its environment is determined by the emitted thermal [longwave (LW)] flux and the reflected part of the solar irradiance [shortwave (SW)] flux at the top of the atmosphere (TOA). Equilibrium of Earth's climate requires that the global annual mean net radiation flux at the TOA be approximately zero.

Clouds and the Earth's Radiant Energy System (CERES) (*1*) instruments on the Tropical Rainfall Measuring Mission (TRMM, begun in 1998) satellite and the Earth Observing System Terra (begun in 2000) satellite have observed LW fluxes 5 to 10 W m^{-2} (~2 to 4%) higher than those from the Earth Radiation Budget Experiment (ERBE) (*2*) scanner data (1985–1989). These differences cannot be fully explained by known changes of the satellite observation systems (*3*–*5*). The ERBE wide field of view (WFOV) data (1985–1995) span a longer time period though at lower spatial resolution than the ERBE scanner data and clearly show a decadal increase of LW flux, primarily during the first half of the 1990s (*3*) (Fig. 1). Local LW changes are weakly positive, about 4 W m^{-2} over 10 years, in most of the tropics (*6*). Much larger changes occur adjacently with opposite sign (for example, the West Pacific warm pool and Central Pacific region).

Empirical orthogonal function (EOF) analysis decomposes temporal variations into orthogonal spatial patterns that sometimes reveal independent physical mechanisms (*7*). When EOF analysis is applied to the radiation flux anomalies (*8*), the first principal component (PC) describing the time evolution of the first spatial pattern is strongly correlated with the NINO3 El Niño–Southern Oscillation (ENSO) index (*9*), and the first spatial pattern explaining the largest fraction of the temporal variance resembles the West Pacific–Central Pacific dipole. This mode is an embodiment of the well-known shift of the convection center between the two regions in different ENSO phases (*10*). But the decadal LW flux increase (Fig. 1) cannot be identified by the spatial-temporal EOF decomposition. Although in 1998 both the ENSO index and the tropical mean LW flux anomalies reach their maximum, the two time series are poorly correlated with each other (Fig. 2A). This implies that the mechanism behind the long-term average LW flux increase is distinct from the ENSO phenomenon. The elevated CERES Terra LW flux in 2000, a non-ENSO year, relative to the ERBE period is further evidence for a longer term flux variation.

Because ENSO primarily involves a spatial redistribution, frequency histograms of SW and LW fluxes covering the entire tropics exhibit much less interannual variability than do the geographical distributions of the fluxes within the tropics. We therefore minimize the ENSO signal by constructing a SW-LW joint frequency distribution (JFD) matrix (*11*) for each month. We then compute anomalies of the JFD with respect to the climatology and decompose these with EOF analysis (*12*). The high correlation between the first PC and the tropical mean LW flux anomaly time series means that the first mode of the SW-LW JFD EOF represents the long-term increase in LW flux (Fig. 2A). The first PC shows that the increase begins at the start of the 1990s, and elevated flux levels are still present in 2000. The first JFD EOF pattern (Fig. 2B) shows that occurrences of LW flux values of ~255 W m^{-2} and SW flux values of ~75 W m^{-2} decrease over the 1985–2000 time period and are replaced by higher LW fluxes of ~290 W m^{-2} and lower SW fluxes of ~60 W m^{-2}. To mimic the effect of a worst-case hypothetical calibration shift in

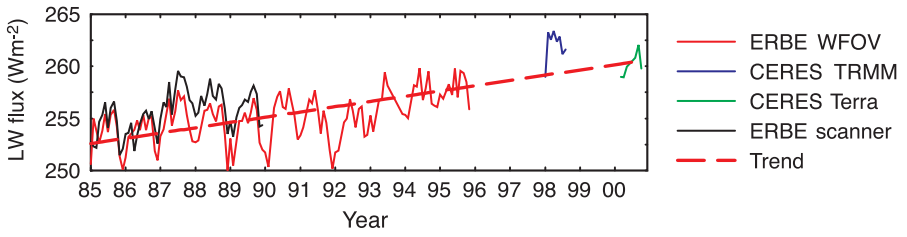

Fig. 1. Tropical mean LW flux time series showing decadal variation averaged over 30°S–30°N. The red dashed line is the linear fit to the ERBE WFOV, CERES TRMM, and CERES Terra data. The slope

[1]Department of Earth and Environmental Sciences, Columbia University, Palisades, NY 10964, USA. [2]NASA/Goddard Institute for Space Studies, 2880 Broadway, New York, NY 10025, USA.

*To whom correspondence should be addressed. E-

DOCKET ALARM

Explore Litigation Insights

Docket Alarm provides insights to develop a more informed litigation strategy and the peace of mind of knowing you're on top of things.

Real-Time Litigation Alerts

Keep your litigation team up-to-date with **real-time alerts** and advanced team management tools built for the enterprise, all while greatly reducing PACER spend.

Our comprehensive service means we can handle Federal, State, and Administrative courts across the country.

Advanced Docket Research

With over 230 million records, Docket Alarm's cloud-native docket research platform finds what other services can't. Coverage includes Federal, State, plus PTAB, TTAB, ITC and NLRB decisions, all in one place.

Identify arguments that have been successful in the past with full text, pinpoint searching. Link to case law cited within any court document via Fastcase.

Analytics At Your Fingertips

Learn what happened the last time a particular judge, opposing counsel or company faced cases similar to yours.

Advanced out-of-the-box PTAB and TTAB analytics are always at your fingertips.

API

Docket Alarm offers a powerful API (application programming interface) to developers that want to integrate case filings into their apps.

LAW FIRMS
Build custom dashboards for your attorneys and clients with live data direct from the court.

Automate many repetitive legal tasks like conflict checks, document management, and marketing.

FINANCIAL INSTITUTIONS
Litigation and bankruptcy checks for companies and debtors.

E-DISCOVERY AND LEGAL VENDORS
Sync your system to PACER to automate legal marketing.